https://doi.org/10.5194/egusphere-2023-1711
Preprint. Discussion started: 18 August 2023

Fast uplift in the Southern Patagonian Andes due to long and short term deglaciation and the asthenospheric window underneath

Veleda A. P. Muller[1], Pietro Sternai[1], Christian Sue[2,3]

[1] Dipartimento di Scienze dell'Ambiente e della Terra (DISAT), Università degli Studi di Milano-Bicocca, Piazza della Scienza 4, Milan, Italy
[2] Institute des Sciences de la Terre (ISTerre), Université Grenoble Alpes, Université Savoie Mont Blanc, CNRS, IRD, IFSTTAR, Université Gustave Eiffel, Grenoble, France.
[3] Université de Franche Comté, Besançon, France.
Correspondence to: Veleda A.P. Muller (v.paivamuller@campus.unimib.it)

Abstract. An asthenospheric window underneath much of the South American continent increases the heat flow in the Southern Patagonian Andes, where glacial-interglacial cycles drive the building and melting of the Patagonian Icefields since the latest Miocene. The Last Glacial Maximum (LGM) was reached ~20000 years ago, and an acceleration of the deglaciation rate is recorded since the Little Ice Age (LIA), ~400 years ago. Fast uplift rates of up to 41±3 mm/yr are measured by GNSS around the Southern Patagonian Icefield and currently ascribed to post-LIA lithospheric rebound, but the possible longer-term post-LGM rebound is poorly constrained. These uplift rates, in addition, are one order of magnitude higher than those measured on other glaciated orogens (e.g., the European Alps), which raises questions about the role of the asthenospheric window in affecting the vertical surface displacement rates. Here, we perform geodynamic thermo-mechanical numerical modelling to estimate the surface uplift rates induced by post-LIA and post-LGM deglaciation accounting for temperature dependent rheologies and different thermal regimes in the asthenosphere. Our modelled maximum postglacial rebound matches the observed uplift rate budget only when both post-LIA and post-LGM deglaciation are accounted for and if a standard continental mantle potential temperature is increased by 150-200 °C. The asthenospheric window thus plays a key role in controlling the magnitude of presently observed uplift rates in the Southern Patagonian Andes.

1 Introduction

Vertical displacements of the Earth's surface with respect to the geoid occur in response to the motion of crustal and mantle rock masses due to plate tectonics and the associated redistribution of sediments, water, and ice by surface processes (e.g., Molnar and England, 1990; Watts, 2001; Champagnac et al., 2012; Sternai, 2023; Cloetingh et al., 2023). For instance, excess of topography in orogenic regions due to convergence and crustal stacking deflects the lithosphere downward, whereas unloading by erosion and ice melting causes upward deflection of the lithosphere, known as "isostatic" adjustment (e.g., Peltier and Andrews, 1976; Peltier, 1996, 2004; Mitrovica and Forte, 1997; Butler and Peltier, 2000; Kaufman and Lambeck, 2002; Watts, 2001; Turcotte and Schubert, 2002). The magnitude of surface uplift rates is set primarily by the lithosphere and asthenosphere viscosities, which depend, amongst other factors, on the thermal field at depth (McKenzie and Richter, 1981; McKenzie and Bickle, 1988; Gurnis, 1989; Ranalli, 1995, 1997; Kaufman et al., 1997; Watts, 2001; Turcotte and Schubert, 2002). Although the theory that relates surface ice load changes and isostatic adjustment is well developed (e.g., Peltier and Andrews, 1976; Peltier, 1996, 2004; Mitrovica and Forte, 1997; Kaufman and Lambeck, 2002; Stuhne and Peltier, 2015; Van der Wal et al., 2015), recognizing and quantifying expressions of such dynamics in natural settings is difficult.

The Southern Patagonian Andes in the South American Continent are located above a transition zone between the subducting Antarctic and Nazca plates and a wide asthenospheric window (Fig. 1a; Cande and Leslie, 1986). The Chile Triple Junction (CTJ) at ~46 °S delimits the surface tip of the asthenospheric window, which opened during the last ~16 Ma from south to north (Ramos and Kay, 1992; Breitsprecher and Thorkelson, 2009). First order effects of the asthenospheric flow on the surface continental geology are the inhibition of arc volcanism in favour of retroarc magmatism, forward propagation of the fold-and-thrust belt, and rock uplift (Ramos and Kay, 1992; Ramos, 2005; Breitsprecher and Thorkelson, 2009; Guillaume et al., 2009; Lagabrielle et al., 2010; Georgieva et al., 2016). Rock uplift due to asthenospheric upwelling, in particular, was estimated as < 0.15 mm/yr in the last 3 Ma over an area of about 100000 km^2 around the CTJ latitude (Guillaume et al., 2009). The heat flow was calculated as >100 mW/m^2 near the CTJ, ~70-90 mW/m^2 in the center of the asthenospheric window (~50 °S), and 50-60 mW/m^2 near its northern boundary (~46 °S) (Ávila and Dávila, 2018), suggesting that the mantle temperature beneath Southern Patagonia is likely higher than in normal subduction zones (Ranalli, 1997).

The Patagonian Ice Sheet covered the Southern Patagonian Andes between ~30000 and ~17000 years ago, extending from latitudes 38 to 55 °S with estimated area of ~490000 km^2 and volume of ~550000 km^3 (Fig. 1 a) based on preserved glacial geomorphologies, stratigraphic and paleoecological records, and geochronological data (Moreno et al., 1999, 2005; McCulloch et al., 2000, 2005; Hulton et al., 2002; Rabassa, 2008; Glasser et al., 2005, 2016; Glasser and Jansson, 2008; Hein et al., 2010; Boex et al, 2013; Bourgois et al., 2016; Martinod et al., 2016; Bendle et al., 2017; Thorndycraft et al., 2019; Davies et al., 2020). The average and maximum ice thickness were estimated as ~1100 m and ~2500 m, respectively (McCulloch et al., 2000; Hulton et al., 2002; Boex et al., 2013; Davies et al., 2020). Currently, the SPI covers an area of ~13219 km^2 with a volume of 3632 ± 675 km^3, whereas the Northern Patagonian Icefield (NPI) covers an area of ~3976 km^2 with a volume of 1124 ± 260 km^3 (Fig. 1). The present-day ice thickness reaches up to ~2000 m in deep glacial valleys (Millan et al., 2019). The long term ice loss rate is uncertain, but more than 75% of ice was certainly lost since the Last Glacial Maximum (LGM, approximately 20000 years ago), and some models predicted more than 95% of ice loss with separation between the SPI and NPI in the first 5000 to 10000 years of post-LGM deglaciation (McCulloch et al., 2000; Hulton et al., 2002; Boex et al., 2013; Bourgois et al., 2016; Thorndycraft et al., 2019; Davies et al., 2020).

GNSS and remote sensing data show ongoing vertical rock uplift rates between 30±3 and 41±3 mm/yr in the northern part of the Southern Patagonian Icefield (SPI, Fig. 1b), gradually decreasing toward its peripheral parts (Aniya, 1996; Aniya et al., 1997; Rignot et al., 2003; Ivins and James, 1999, 2004; Dietrich et al., 2010; Willis et al., 2012; Lange et al., 2014). Such outstandingly high uplift rates are currently ascribed to lithospheric viscoelastic glacial isostatic adjustment (GIA) following the Little Ice Age (LIA), with apex around 1630 AD (Ivins and James, 1999, 2004; Glasser et al., 2011). Deglaciation since the LIA was responsible for an ice loss of 503 ± 101.1 km^3 in the SPI (Glasser et al., 2011), with a substantial increase of the glacial recession after the 20th century (Aniya, 1996; Aniya et al., 1997; Rignot et al., 2003; Glasser et al., 2011; Davies and Glasser, 2012; Ivins et al., 2011; Willis et al., 2012). To match the very high observed uplift rate budget, previous GIA studies infer low asthenosphere viscosity (in the order of 10^{18} Pa s) and thin elastic lithosphere (~35 km thick) (Ivins and James, 1999, 2004; Klemann et al., 2007; Dietrich et al., 2010; Lange et al, 2014). However, although this is consistent with abnormally high mantle temperatures, viscosity estimates from previous studies are untied to the regional thermal regime, which prevents a more thorough characterization of the role of the asthenospheric window underneath the SPI in affecting the observed uplift rates. In addition, the contribution of post-LGM deglaciation to present-day rock uplift rate was marginally addressed. Here, we perform fully coupled thermo-mechanical numerical geodynamic experiments forced by surface unloading scaled on post-LIA and post-LGM ice melting to evaluate their relative contribution to the observed regional uplift rates. Numerical experiments account for a range of positive thermal anomalies in the asthenosphere to further asses the role of the asthenospheric window in setting the mantle viscosity and associated postglacial rebound. Focusing on the magnitude, rather than the pattern, of the inferred surface uplift rates, we use the observed budget of rock uplift rate to constrain plausible thermal and viscosity structures at depth as well as the timing of postglacial rebound.

2 Methodology

2.1 Numerical model

We use a fully coupled thermo-mechanical, visco-elasto-plastic, numerical geodynamic model to quantify the effect of thermal anomalies in the mantle on the magnitude of surface uplift rates due to deglaciation. We provide a short overview of the governing equations hereafter, while a detailed description of numerical technique can be found, for instance, in Gerya and Yuen (2007), Gerya et al. (2019), Sternai (2020), and Muller et al. (2022). The continuity equation allows for the conservation of mass during the displacement of a geological continuum:

$$(1) \qquad \frac{\partial \rho}{\partial t} + \nabla(\rho v) = 0$$

where ρ is the local density, t is time, v is the velocity vector, and ∇ is the divergence operator. The momentum equation describes the changes in velocity of an object in the gravity field due to internal and external forces:

$$(2) \qquad \frac{\partial \sigma_{ij}}{\partial x_i} + \rho g_i = \rho\left(\frac{\partial v_i}{\partial t} + v_j \frac{\partial v_i}{\partial x_j}\right)$$

where σ_{ij} is the stress tensor, x_i and x_j are spatial coordinates, and g_i is the *i*-th component of the gravity vector. The energy equation allows for the conservation of energy during advective and conductive heat transfer in the continuum:

$$(3) \qquad \rho C_P \frac{DT}{Dt} - div(c\nabla T) + v\nabla T = H_r + H_s + H_a + H_l$$

where P is pressure, T is temperature, C_P is specific heat capacity at a constant P, c is the thermal conductivity, $H_r + H_s + H_a + H_l$ are the volumetric heat productions by radiogenic, shear, adiabatic and latent heat, respectively. $H_a \propto \frac{DP}{Dt}$, $H_s = \sigma'_{ij}\dot{\varepsilon}'_{ij(viscous)}$, and H_r and H_l are the radiogenic and latent heat productions.

Ductile deformation is thermally activated generating viscous flow, which involves diffusion and dislocation creep, calculated according to the material shear viscosity:

$$(4) \qquad \frac{1}{\eta_{ductile}} = \frac{1}{\eta_{diff}} + \frac{1}{\eta_{disl}}$$

with

$$\eta_{diff} = \frac{\eta_0}{2\sigma_{cr}^{n-1}} exp\left(\frac{E_a + PV_a}{RT}\right), \text{ and}$$

$$\eta_{disl} = \frac{\eta_0^{\frac{1}{n}}}{2} exp\left(\frac{E_a + PV_a}{nRT}\right) \dot{\varepsilon}_{II}^{\frac{1}{n}-1}$$

where η_{diff} and η_{disl} are the shear viscosity for diffusion and dislocation creep, respectively, η_0 is the material static viscosity, σ_{cr} is the diffusion-dislocation transition critical stress, n is the stress exponent, E_a is the activation energy, V_a is the activation volume, R is the gas constant, and $\dot{\varepsilon}_{II}$ is the second invariant of the strain rate tensor. The viscous deviatoric strain rate tensor, $\dot{\varepsilon}'_{ij\,(viscous)}$, is defined by:

$$(5) \qquad \dot{\varepsilon}'_{ij\,(viscous)} = \frac{1}{2\eta_{ductile}}\sigma'_{ij} + \delta_{ij}\eta_{bulk}\dot{\varepsilon}_{kk} = \frac{1}{2\eta_{diff}}\sigma'_{ij} + \frac{1}{2\eta_{disl}}\sigma'_{ij} + \delta_{ij}\eta_{bulk}\dot{\varepsilon}_{kk}$$

where σ'_{ij} is the deviatoric stress tensor, δ_{ij} is the Kronecker delta, $\dot{\varepsilon}_{kk}$ is the volumetric strain rate (e.g., related to phase transformations), and η_{bulk} is the bulk viscosity. Recoverable deformation is defined by the elastic deviatoric strain rate tensor, $\dot{\varepsilon}'_{ij\,(elastic)}$, as:

$$(6) \qquad \dot{\varepsilon}'_{ij\,(elastic)} = \frac{1}{2\mu}\frac{\breve{D}\sigma'_{ij}}{Dt}$$

where μ is the shear modulus and $\frac{\breve{D}\sigma'_{ij}}{Dt}$ is the objective co-rotational time derivative of the deviatoric stress tensor. The plastic deformation, brittle and localised, occurs at low temperature when the absolute shear stress limit, σ_{yield}, is reached, with

$$(7) \qquad \sigma_{yield} = C + \sin(\varphi)P$$

where C is cohesion and φ is the effective internal friction angle. The plastic strain rate tensor, $\dot{\varepsilon}'_{ij\,(plastic)}$, is defined as:

$$(8) \qquad \dot{\varepsilon}'_{ij\,(plastic)} = 0 \; for \; \sigma_{II} < \sigma_{yield}, \; \dot{\varepsilon}'_{ij\,(plastic)} = \mathcal{X}\frac{\partial\sigma'_{ij}}{2\sigma_{II}} \; for \; \sigma_{II} \geq \sigma_{yield}$$

where $\mathcal{X}$ is the plastic multiplier which satisfies the plastic yielding condition $\sigma_{II} = \sigma_{yield}$. The bulk strain rate tensor, $\dot{\varepsilon}'_{ij(bulk)}$, integrates the viscous, elastic and plastic deformation:

https://doi.org/10.5194/egusphere-2023-1711
Preprint. Discussion started: 18 August 2023

$$\dot{\varepsilon}'_{ij(bulk)} = \dot{\varepsilon}'_{ij(viscous)} + \dot{\varepsilon}'_{ij(elastic)} + \dot{\varepsilon}'_{ij(plastic)} \quad (9)$$

2.2 Reference model setup and modeling approach

The model domain, scaled on the study region, is 700 km wide and 120 km thick. From top to bottom, the model accounts for 10 km of 'sticky' air, 30 km of continental crust (with rheology of quartzite, Ranalli, 1995), 30 km of lithospheric mantle, and 50 km of asthenospheric mantle (with rheology of dry dunite, Ranalli, 1995), in agreement with literature data (e.g., Klemann et al., 2007). The initial geotherm is piece-wise linear resulting from an adiabatic temperature gradient of 0.5 °C/km in the asthenosphere (Turcotte and Schubert, 2002) and thermal boundary conditions equal to 0 °C at the surface and 1327 °C at the bottom of the lithosphere, with nil horizontal heat flux across the vertical boundaries. The rheologic and thermal structure of the reference model give a lithospheric elastic thickness, *Te* (*sensu* Burov and Diament, 1995), of ~30 km, comparable to previous estimates underneath the SPI based on GIA models (Ivins and James, 1999; Dietrich et al., 2010; Lange et al., 2014), heat flow data (Ávila and Dávila, 2018), and waveform inversion (Robertson Maurice et al., 2003). Rocks rheological properties are listed in Table 1.

The numerical model uses the finite differences with marker-in-cell technique, resolved by 51 × 61 nodes in x and y directions, respectively, distributed on a Eulerian grid that accounts for a maximum resolution of 1 km along the y direction in the upper part of the model domain, and ~13 km in the x direction. 400 × 400 Lagrangian markers are randomly distributed along the x and y dimensions and used for advecting the material properties (Gerya and Yuen, 2007; Gerya et al., 2019). The material properties carried by Lagrangian markers are then interpolated onto the Eulerian grid via a 4th order Runge-Kutta interpolation scheme. An internal free surface is simulated through the 10 km thick layer of sticky air. The velocity boundary conditions are free slip at all boundaries (x = 0 and x = 700 km; y = 0 and y = 120 km).

On the top of the crust and in the middle of the model domain we impose a 2 km thick pseudo-icecap to simulate lithospheric unloading during deglaciation. The pseudo-icecap is 70 km wide for the post-LIA model set and 200 km wide for the post-LGM model sets (Fig. 2 a). We compute the surface load, *L*, as

$$L = \rho_{ice} g h_{ice}, \quad (10)$$

where ρ_{ice} is the pseudo-icecap density, g is the gravity acceleration, and h_{ice} is the pseudo-icecap thickness, and deglaciation occurs by gradually reducing h_{ice} in time (Fig. 2 b, c). We run two sets of experiments for the post-LGM deglaciation. In *Model set 1,* 75% of ice loss

https://doi.org/10.5194/egusphere-2023-1711
Preprint. Discussion started: 18 August 2023

occurs in 20000 years (i.e., 1500 m drop of ice thickness, Fig. 2 b), thus assuming a conservative estimate of ice loss since the beginning of the LGM until the present-day. In *Model set 2*, 95% of ice loss occurs in 10000 years (i.e., 1900 m drop of ice thickness, Fig. 2 b), assuming faster deglaciation rates of the Patagonian Ice Sheet in the first half of post-LGM deglaciation (McCulloch et al., 2000; Hulton et al., 2002; Boex et al., 2013; Bendle et al., 2017; Thorndycraft et al., 2019; Davies et al., 2020). For the post-LIA deglaciation, we simulate 10% of ice loss in 400 years (i.e., 200 m drop of ice thickness, Fig. 2 c) (Aniya, 1996; Aniya et al., 1997; Rignot et al., 2003; Ivins and James, 1999, 2004; Dietrich et al., 2010; Willis et al., 2012; Lange et al., 2014).

In the models the initial lateral extent of the pseudo-icecap does not change throughout the deglaciation. Although this simplification may affect the inferred pattern of postglacial rebound, it greatly facilitates the simulation of deglacial lithospheric unloading without significantly affecting the magnitude of postglacial rebound, which is the main focus here. All simulations account for some spin up time before the deglaciation begins, so that the lithosphere-asthenosphere system adjusts to the pseudo-icecap initial load. The surface uplift rate during the deglaciation is calculated through time as the surface elevation change resulting from the modelled strain field divided by the viscoelastic timestep. Given the geologically short time window investigated here, we neglect deformation related to longer term tectonic forces. The parametric study focuses on the mantle potential temperature (*sensu* McKenzie and Bickle, 1988) which accounts for positive thermal anomalies, TA, of up to 200 °C in steps of 50 ° C, added to the reference mantle potential temperature of 1265 °C (McKenzie and Bickle, 1988; Currie and Hyndman, 2006; Ávila and Dávila, 2018; Sternai, 2020) to mimic the presence of a slab window at depth.

https://doi.org/10.5194/egusphere-2023-1711
Preprint. Discussion started: 18 August 2023

3 Results

Results are shown in Table 2 and Figs. 4-7. In agreement with the theory of lithospheric flexure (e.g., Turcotte and Schubert, 2002) the deglaciation triggers uplift in the region covered by the melting pseudo-icecap and subsidence in the neighbouring regions (Figs. 4-6). Overall, increasing the mantle potential temperature decreases the asthenospheric viscosity, with significant effects on the magnitude of the modelled surface velocity field. The asthenosphere viscosity ranges between 10^{22}-10^{19} Pa s in simulations with TA equal to 0 (reference model), 50 and 100 °C, and between 10^{19}-10^{16} Pa s in simulations with TA equal to 150 and 200 °C (Fig. 3 a-d). Lithospheric warming due to increasing mantle potential temperature also leads to a reduction of the lower lithosphere viscosity (from 10^{22} to 10^{20} Pa s), thereby decreasing the integrated lithospheric strength.

In *Model set 1* for Post-LGM deglaciation, when TA is 0 (reference model) the maximum uplift rates is < 1 mm/yr during the first 5000 years of the deglaciation, increasing gradually up to 9.5 mm/yr in the later stages of the deglaciation (i.e., 20000 years, Fig. 4). When TA equals 50, 100, 150 and 200 °C, the maximum uplift rates can reach up to ~2, ~5, ~12, and ~15 mm/yr, respectively, already in the first 1000 years of the deglaciation (Fig. 4 a). When TA is 50 and 100 °C the maximum uplift rate is subject to a protracted increase in time, reaching up to ~12 and ~14 mm/yr after 20000 years of deglaciation (Figs. 4 b-d and 7 a). For TA equal to 150 and 200 °C, the maximum uplift rate reach a plateau between 11 and 17 mm/yr during the 20000 years of deglaciation (Figs. 4 and 7 a, Table 2). After the end of the deglaciation, the maximum uplift rate takes longer than about 5000 years to re-equilibrate to 0 mm/yr when TA ≤ 100 °C, whereas it drops to 0 mm/yr almost immediately when TA is 150 or 200 °C (Fig. 7 a).

In the *Model set 2* for Post-LGM deglaciation, the maximum uplift rate is less than 2 mm/yr during the first 1000 years of deglaciation when TA is 0, 50 and 100 °C, whereas it reaches up to ~22 and ~30 mm/yr during in the first 1000 years of deglaciation when TA is 150 and 200 °C (Fig. 5 a, 7 b, and Table 2). Between 5000 and 10000 years of deglaciation, the maximum uplift rate increases to ~19, ~25 and ~36 mm/yr, respectively when TA is 0, 50 and 100 °C, whereas it reach up to between 36 and 41 mm/yr between 50000 and 1000 years of deglaciation when TA equal to 150 and 200 °C. The maximum uplift rate decreases slower if TA is 0, 50 and 100 °C, taking longer than 5000 year after the deglaciation to drop to values <5 mm/yr (Fig. 7 b and Table 2), whereas it quickly drops to < 2 mm/yr when the deglaciation is over and TA is 150 and 200°C (Figs. 5 b-d and 7b). Overall, a warmer and

https://doi.org/10.5194/egusphere-2023-1711
Preprint. Discussion started: 18 August 2023

less viscous asthenosphere generates a higher magnitude and fast changing postglacial rebound than a cooler and more viscous asthenosphere.

In the post-LIA model set, the maximum uplift rate is ~1.4, ~2.3 and ~2.2 mm/yr during the first 100 years of deglaciation when TA is respectively 0, 50, and 100 °C, whereas it reaches ~8.3 and ~23 mm/yr during the same interval when TA is respectively 150 and 200 °C (Figs. 6 a, 7 c, and Table 2). Between 200 and 400 years of deglaciation, the maximum uplift rate reaches ~1.9, ~2.5 and ~3 mm/yr when TA equal to 0, 50 and 100 °C, and ~14 and ~25.5 mm/yr when TA is 150 and 200 °C, respectively (Figs. 6 c-d, 7 c, and Table 2). When the deglaciation ends, the maximum uplift rate drops to ~0 mm/yr in ~ 100 years when TA ≤ 100 °C, whereas it takes longer than 1000 years when TA equals 150 °C or 200 °C (Fig. 7 c). Overall, a warmer and less viscous asthenosphere generates a higher magnitude postglacial rebound which, however, takes much longer to re-equilibrate to 0 mm/yr after the end of the deglaciation than a cooler and more viscous asthenosphere.

4 Discussion and conclusions

Our modelling is simplistic in that we impose a linear and uniform ice loss instead of a more realistic ice-sheet melting pattern in space and time. This choice is motivated by the limited data reporting on the SPI melting velocities and associated redistribution of the surface masses, which cover time spans much shorter than the post-LIA and post-LGM time windows investigated here (Aniya, 1996; Aniya et al., 1997; Rignot et al., 2003; Ivins and James, 1999, 2004; Willis et al., 2012; Dietrich et al., 2010; Lange et al., 2014). As previously highlighted (Hulton et al., 2002; Rabassa, 2008; Glasser et al., 2011; Davis and Glasser, 2012; Martinod et al., 2016; Bendle et al., 2017; Davies et al., 2020), constraints regarding the ice-sheet mass balance and melting velocities throughout the time windows of interest are difficult to obtain from the preserved geomorphological, stratigraphic and geochronological records. We also assume a homogeneous lithosphere and neglect lateral viscosity variations in the asthenosphere (Klemann et al., 2007) despite the long-term southern Andean orogenic history (Cande and Leslie, 1986; Ramos, 2005; Muller et al., 2021). Notwithstanding these limitations, however, our fully coupled numerical thermo-mechanical geodynamic models provide realistic uplift rates that one can compare to current geodetic observations. Following the example of previous studies (Ivins and James, 1999, 2004; Klemann et al., 2007; Dietrich et al., 2010; Lange et al., 2014), we discuss our results assuming that GNSS-measured rock uplift rates are mostly related to the deglaciation history and only marginally controlled by the longer term geodynamics (e.g., Ramos, 2005; Muller et al., 2021).

We first remark that inferred maximum post-LIA uplift rate of up to a few mm/yr from experiments without or with a low asthenospheric thermal anomaly (TA ≤ 100 °C) are within the same order of magnitude of maximum uplift rates measured in collisional orogens such as the European Alps (Sue et al., 2007; Serpelloni et al., 2013; Walpersdorf et al., 2015; Sternai et al., 2019) and the Himalayas (Larson et al., 1999). Since these collisional orogens are characterized by a thicker lithosphere (Geissler et al., 2010; Ravikumar et al., 2020), they are likely less sensitive to mantle dynamics than the Southern Patagonian Andes. When we consider lithospheric unloading due to post-LGM deglaciation of a wider ice sheet, however, the inferred maximum uplift rate via *Model set 1* and *Model set 2* reaches up to 10 mm/yr for and 20 mm/yr, respectively, even without asthenospheric thermal anomaly. This suggests a that a contribution from long-term postglacial rebound to the present-day uplift rates measured in the SPI is likely.

In the Southern Patagonian Andes, the regional asthenosphere viscosity was estimated between 1.6 and 8×10^{18} Pa s from GIA models based on GNSS and satellite observations (Ivins and James, 1999, 2004; Klemann et al., 2007; Dietrich et al., 2010; Willis et al., 2012; Lange et al., 2014). Similarly, the asthenosphere viscosity from our models when TA > 100 °C is $< 10^{19}$ Pa s, with the lowest viscosity value of 10^{16} Pa s imposed where partial melting, supported by the regional Holocene volcanism (Stern and Kilian, 1996), occurs. Under these conditions, however, our experiments provide uplift rates between 14 and 26 mm/yr for post-LIA deglaciation indicating that, even with a very low viscosity asthenosphere, the rebound due to the short-term post-LIA deglaciation does not reach the presently observed maximum uplift rates of 41 ± 3 mm/yr. Experiments that account for a low viscosity asthenosphere and long-term post-LGM deglaciation lasting for 20000 years and 10000 years reach up to ~25 and ~42 mm/yr of uplift rate, respectively, comparable to present-day values. Results, therefore, indicate that the outstanding observational budget of rock uplift in the SPI is matched only when accounting for higher-than-normal mantle temperatures, thereby highlighting the relevance of the regional asthenospheric window.

Because of the limited knowledge regarding the timing and amount of ice loss since the LGM (e.g., Davies et al., 2020), it is difficult to position in time present-day uplift rate measurements within the investigated deglaciation scenarios to assess the contribution of post-LGM and post-LIA deglaciation to the maximum uplift rate budget. In the faster post-LGM deglaciation scenario (*Model set 2*) the observed maximum uplift rate budget is attained in about 10000 years of deglaciation, but only minor residual rebound could be observed today regardless of the amount of ice loss (Fig. 7 b). If post-LGM deglaciation occurred slower (*Model set 1*), this event may contribute to up to 40% to the present-day uplift rate budget. Although it is difficult to reconcile this scenario with the geomorphological and geochronological evidences (Hulton et al., 2002; Boex et al., 2013; Davis and Glasser, 2012; Martinod et al., 2016; Bendle et al., 2017; Thorndycraft et al., 2019; Davies et al., 2020), it appears that post-LIA rebound alone cannot cover the entire budget of the observed uplift rates even with the highest tested TA, which points to a non-negligible contribution from post-LGM deglaciation. This latter conclusion is reinforced by estimates of the mantle relaxation time, τ_r, as (Turcotte and Schubert, 2002):

$$\tau_r = \frac{4\pi v}{g\lambda}, \tag{11}$$

where v is the asthenosphere viscosity, λ is the width of the ice sheet, and g is the gravity acceleration. Using $10^{16}<v<10^{18}$ Pa s and λ =200 km leads to ~2000<τ_r<~200000 years, a time range considerably longer than the post-LIA deglaciation and including full Pleistocene glacial-interglacial cycles (Ruddiman et al., 1986). We therefore propose that currently observed uplift rates in the Southern Andes are driven by both post-LGM and post LIA lithospheric rebound enhanced by a thermal anomaly of at least 150 °C due to the regional asthenospheric window which lowers mantle viscosities.

As a final consideration, our models suggest that we shall measure regional uplift rates in the order of the tens of cm/yr in the next century if the currently observed ice loss rate of at least -20 Gt/yr in the SPI (Willis et al., 2012) will continue until the total meltdown of the ice sheet in ~200 years.

5 Acknowledgements

This work was supported by the Italian Ministry of Education, MUR (Project Dipartimenti di Eccellenza 2023-2027, TECLA, Department of Earth and Environmental Sciences, University of Milano-Bicocca), and the Fondazione Cariplo and Fondazione CDP (Grant n° 2022 – 1546_001). The Université Grenoble Alpes and the French CNRS also supported this work.

References

Aniya, M. (1996). Holocene variations of Ameghino glacier, southern Patagonia. *The Holocene*, *6*(2), 247-252.

Aniya, M., Sato, H., Naruse, R., Skvarca, P., & Casassa, G. (1997). Recent glacier variations in the Southern Patagonia icefield, South America. *Arctic and Alpine Research*, *29*(1), 1-12.

Ávila, P., & Dávila, F. M. (2018). Heat flow and lithospheric thickness analysis in the Patagonian asthenospheric windows, southern South America. *Tectonophysics*, *747*, 99-107.

Bendle, J. M., Palmer, A. P., Thorndycraft, V. R., & Matthews, I. P. (2017). High-resolution chronology for deglaciation of the Patagonian Ice Sheet at Lago Buenos Aires (46.5 S) revealed through varve chronology and Bayesian age modelling. *Quaternary Science Reviews*, *177*, 314-339.

Boex, J., Fogwill, C., Harrison, S., Glasser, N. F., Hein, A., Schnabel, C., & Xu, S. (2013). Rapid thinning of the late Pleistocene Patagonian Ice Sheet followed migration of the Southern Westerlies. *Scientific Reports*, *3*(1), 1-6.

Bourgois, J., Cisternas, M. E., Braucher, R., Bourlès, D., & Frutos, J. (2016). Geomorphic records along the general Carrera (Chile)–Buenos Aires (Argentina) glacial lake (46–48 S), climate inferences, and glacial rebound for the past 7–9 ka. *The Journal of Geology*, *124*(1), 27-53.

Breitsprecher, K., & Thorkelson, D. J. (2009). Neogene kinematic history of Nazca–Antarctic–Phoenix slab windows beneath Patagonia and the Antarctic Peninsula. *Tectonophysics*, *464*(1-4), 10-20.

Burov, E. B., & Diament, M. (1995). The effective elastic thickness (T e) of continental lithosphere: What does it really mean?. *Journal of Geophysical Research: Solid Earth*, *100*(B3), 3905-3927.

Butler, S. L., & Peltier, W. R. (2000). On scaling relations in time-dependent mantle convection and the heat transfer constraint on layering. *Journal of Geophysical Research: Solid Earth*, *105*(B2), 3175-3208.

Cande, S. C., & Leslie, R. B. (1986). Late Cenozoic tectonics of the southern Chile trench. *Journal of Geophysical Research: Solid Earth*, *91*(B1), 471-496.

Champagnac, J. D., Molnar, P., Sue, C., & Herman, F. (2012). Tectonics, climate, and mountain topography. *Journal of Geophysical Research: Solid Earth*, *117*(B2).

Cloetingh, S., Sternai, P., Koptev, A., Ehlers, T. A., Gerya, T., Kovács, I., Oerlemans, J., Beekman, F., Lavallée, Y., Dingwell, D., Békési, E., Porkolàb, K., Tesauro, M., Lavecchia, A., Botsyun, S., Muller, V., Roure, F., Serpelloni, E., Matenco, L., Castelltort, S., Giovannelli, D., Brovarone, A.V., Malaspina, N., Coletti, G., Valla, P., & Limberger, J. (2023). Coupled surface to deep Earth processes: Perspectives from TOPO-EUROPE with an emphasis on climate-and energy-related societal challenges. *Global and Planetary Change*, 104140.

Currie, C. A., & Hyndman, R. D. (2006). The thermal structure of subduction zone back arcs. *Journal of Geophysical Research: Solid Earth*, *111*(B8).

Davies, B. J., & Glasser, N. F. (2012). Accelerating shrinkage of Patagonian glaciers from the Little Ice Age (~ AD 1870) to 2011. *Journal of Glaciology*, *58*(212), 1063-1084.

Davies, B. J., Darvill, C. M., Lovell, H., Bendle, J. M., Dowdeswell, J. A., Fabel, D., García, J.-L., Geiger, A., Glasser, N.F., Gheorghiu, D.M., Harrison, S., Hein, A.S., Kaplan, M.R., Martin, J.R.V., Mendelova, M., Palmer, A., Pelto, M., Rodés, A., Segredo, E.A., Smedley, R.K., Smellie J., & Thorndycraft, V. R. (2020). The evolution of the Patagonian Ice Sheet from 35 ka to the present day (PATICE). *Earth-Science Reviews*, *204*, 103152.

Dietrich, R., Ivins, E. R., Casassa, G., Lange, H., Wendt, J., & Fritsche, M. (2010). Rapid crustal uplift in Patagonia due to enhanced ice loss. *Earth and Planetary Science Letters*, *289*(1-2), 22-29.

Geissler, W. H., Sodoudi, F., & Kind, R. (2010). Thickness of the central and eastern European lithosphere as seen by S receiver functions. *Geophysical Journal International*, *181*(2), 604-634.

Georgieva, V., Melnick, D., Schildgen, T. F., Ehlers, T. A., Lagabrielle, Y., Enkelmann, E., & Strecker, M. R. (2016). Tectonic control on rock uplift, exhumation, and topography above an oceanic ridge collision: Southern Patagonian Andes (47 S), Chile. *Tectonics*, *35*(6), 1317-1341.

Gerya, T. (2019). *Introduction to numerical geodynamic modelling*. Cambridge University Press.

Gerya, T. V., & Yuen, D. A. (2007). Robust characteristics method for modelling multiphase visco-elasto-plastic thermo-mechanical problems. *Physics of the Earth and Planetary Interiors*, *163*(1-4), 83-105.

Glasser, N. F., Harrison, S., Jansson, K. N., Anderson, K., & Cowley, A. (2011). Global sea-level contribution from the Patagonian Icefields since the Little Ice Age maximum. *Nature Geoscience*, *4*(5), 303-307.

Glasser, N. F., Jansson, K. N., Harrison, S., & Rivera, A. (2005). Geomorphological evidence for variations of the North Patagonian Icefield during the Holocene. *Geomorphology*, *71*(3-4), 263-277.

Glasser, N., & Jansson, K. (2008). The glacial map of southern South America. *Journal of Maps*, *4*(1), 175-196.

Glasser, N. F., Jansson, K. N., Duller, G. A., Singarayer, J., Holloway, M., & Harrison, S. (2016). Glacial lake drainage in Patagonia (13-8 kyr) and response of the adjacent Pacific Ocean. *Scientific reports*, *6*(1), 21064.

Guillaume, B., Martinod, J., Husson, L., Roddaz, M., & Riquelme, R. (2009). Neogene uplift of central eastern Patagonia: dynamic response to active spreading ridge subduction?. *Tectonics*, *28*(2).

Gurnis, M. (1989). A reassessment of the heat transport by variable viscosity convection with plates and lids. *Geophysical Research Letters*, *16*(2), 179-182.

Hein, A. S., Hulton, N. R., Dunai, T. J., Sugden, D. E., Kaplan, M. R., & Xu, S. (2010). The chronology of the Last Glacial Maximum and deglacial events in central Argentine Patagonia. *Quaternary Science Reviews*, *29*(9-10), 1212-1227.

Hirschmann, M. M. (2000). Mantle solidus: Experimental constraints and the effects of peridotite composition. *Geochemistry, Geophysics, Geosystems*, *1*(10).

Hulton, N. R., Purves, R. S., McCulloch, R. D., Sugden, D. E., & Bentley, M. J. (2002). The last glacial maximum and deglaciation in southern South America. *Quaternary Science Reviews*, *21*(1-3), 233-241.

Ivins, E. R., & James, T. S. (1999). Simple models for late Holocene and present-day

https://doi.org/10.5194/egusphere-2023-1711
Preprint. Discussion started: 18 August 2023

Patagonian glacier fluctuations and predictions of a geodetically detectable isostatic response. *Geophysical Journal International*, *138*(3), 601-624.

Ivins, E. R., & James, T. S. (2004). Bedrock response to Llanquihue Holocene and present-day glaciation in southernmost South America. *Geophysical Research Letters*, *31*(24).

Ivins, E. R., Watkins, M. M., Yuan, D. N., Dietrich, R., Casassa, G., & Rülke, A. (2011). On-land ice loss and glacial isostatic adjustment at the Drake Passage: 2003–2009. *Journal of Geophysical Research: Solid Earth*, *116*(B2).

Johannes, W. (1985). The significance of experimental studies for the formation of migmatites. In: *Migmatites*, Ed. Ashworth, J. R. Blackie & Son Ltd, USA Chapman & Hall.

Kaufmann, G., & Lambeck, K. (2002). Glacial isostatic adjustment and the radial viscosity profile from inverse modeling. *Journal of Geophysical Research: Solid Earth*, *107*(B11), ETG-5.

Kaufmann, G., Wu, P., & Wolf, D. (1997). Some effects of lateral heterogeneities in the upper mantle on postglacial land uplift close to continental margins. Geophysical Journal International, 128(1), 175-187.

Klemann, V., Ivins, E. R., Martinec, Z., & Wolf, D. (2007). Models of active glacial isostasy roofing warm subduction: Case of the South Patagonian Ice Field. *Journal of Geophysical Research: Solid Earth*, *112*(B9).

Lagabrielle, Y., Scalabrino, B., Suarez, M., & Ritz, J. F. (2010). Mio-Pliocene glaciations of Central Patagonia: New evidence and tectonic implications. *Andean Geology*, *37*(2), 276-299.

Lange, H., Casassa, G., Ivins, E. R., Schröder, L., Fritsche, M., Richter, A., Groh, A., & Dietrich, R. (2014). Observed crustal uplift near the Southern Patagonian Icefield constrains improved viscoelastic Earth models. *Geophysical Research Letters*, *41*(3), 805-812.

Larson, K. M., Bürgmann, R., Bilham, R., & Freymueller, J. T. (1999). Kinematics of the India-Eurasia collision zone from GPS measurements. *Journal of Geophysical Research: Solid Earth*, *104*(B1), 1077-1093.

Martinod, J., Pouyaud, B., Carretier, S., Guillaume, B., & Hérail, G. (2016). Geomorphic Records along the General Carrera (Chile)–Buenos Aires (Argentina) Glacial Lake (46°–48° S), Climate Inferences, and Glacial Rebound for the Past 7–9 ka: A discussion. The Journal of Geology, 124(5), 631-635.

McCulloch, R. D., Bentley, M. J., Purves, R. S., Hulton, N. R., Sugden, D. E., & Clapperton, C. M. (2000). Climatic inferences from glacial and palaeoecological evidence at the last glacial termination, southern South America. *Journal of Quaternary Science: Published for the Quaternary Research Association*, *15*(4), 409-417.

McCulloch, R. D., Fogwill, C. J., Sugden, D. E., Bentley, M. J., & Kubik, P. W. (2005). Chronology of the last glaciation in central Strait of Magellan and Bahía Inútil, southernmost South America. *Geografiska Annaler: Series A, Physical Geography*, *87*(2), 289-312.

Mckenzie, D. A. N., & Bickle, M. J. (1988). The volume and composition of melt generated by extension of the lithosphere. *Journal of petrology*, *29*(3), 625-679.

McKenzie, D., & Richter, F. M. (1981). Parameterized thermal convection in a layered region and the thermal history of the Earth. *Journal of Geophysical Research: Solid Earth*, *86*(B12), 11667-11680.

Moreno, P. I., Lowell, T. V., Jacobson Jr, G. L., & Denton, G. H. (1999). Abrupt vegetation and climate changes during the last glacial maximum and last termination in the Chilean Lake District: a case study from Canal de la Puntilla (41 S). Geografiska Annaler: Series A, Physical Geography, 81(2), 285-311.

Millan, R., Rignot, E., Rivera, A., Martineau, V., Mouginot, J., Zamora, R., Uribe, J., Lenzano, G., De Fleurian, B., Li, X., Gim, Y., & Kirchner, D. (2019). Ice thickness and bed elevation of the Northern and Southern Patagonian Icefields. *Geophysical Research Letters*, *46*(12), 6626-6635.

Mitrovica, J. X., & Forte, A. M. (1997). Radial profile of mantle viscosity: Results from the joint inversion of convection and postglacial rebound observables. *Journal of Geophysical Research: Solid Earth*, *102*(B2), 2751-2769.

Molnar, P., & England, P. (1990). Late Cenozoic uplift of mountain ranges and global climate change: chicken or egg? *Nature*, *346*(6279), 29-34.

Moreno, P. I., Denton, G. H., Moreno, H., Lowell, T. V., Putnam, A. E., & Kaplan, M. R. (2015). Radiocarbon chronology of the last glacial maximum and its termination in northwestern Patagonia. *Quaternary Science Reviews*, *122*, 233-249.

Muller, V. A., Calderón, M., Fosdick, J. C., Ghiglione, M. C., Cury, L. F., Massonne, H. J., Fanning, M.C., Warren, C.J., Ramírez de Arellano, C., & Sternai, P. (2021). The closure of the Rocas Verdes Basin and early tectono-metamorphic evolution of the Magallanes Fold-and-Thrust Belt, southern Patagonian Andes (52–54° S). *Tectonophysics*, *798*, 228686.

Muller, V. A., Sternai, P., Sue, C., Simon-Labric, T., & Valla, P. G. (2022). Climatic control on the location of continental volcanic arcs. *Scientific Reports*, *12*(1), 1-13.

Peltier, W. R. (1996). Mantle viscosity and ice-age ice sheet topography. *Science*, *273*(5280), 1359-1364.

Peltier, W. R. (2004). Global glacial isostasy and the surface of the ice-age Earth: the ICE-5G (VM2) model and GRACE. *Annu. Rev. Earth Planet. Sci.*, *32*, 111-149.

Peltier, W. R., & Andrews, J. T. (1976). Glacial-isostatic adjustment—I. The forward problem. *Geophysical Journal International*, *46*(3), 605-646.

Rabassa, J. (2008). Late cenozoic glaciations in Patagonia and Tierra del Fuego. *Developments in quaternary sciences*, *11*, 151-204.

Ramos, V. A. (2005). Seismic ridge subduction and topography: Foreland deformation in the Patagonian Andes. *Tectonophysics*, *399*(1-4), 73-86.

Ramos, V. A., & Kay, S. M. (1992). Southern Patagonian plateau basalts and deformation: backarc testimony of ridge collisions. *Tectonophysics*, *205*(1-3), 261-282.

Ranalli, G. (1995). *Rheology of the Earth*. Springer Science & Business Media.

Ranalli, G. (1997). Rheology of the lithosphere in space and time. *Geological Society, London, Special Publications*, *121*(1), 19-37.

Ravikumar, M., Singh, B., Pavan Kumar, V., Satyakumar, A. V., Ramesh, D. S., & Tiwari, V. M. (2020). Lithospheric density structure and effective elastic thickness beneath Himalaya and Tibetan Plateau: Inference from the integrated analysis of gravity, geoid, and topographic data incorporating seismic constraints. *Tectonics*, *39*(10), e2020TC006219.

Rignot, E., Rivera, A., & Casassa, G. (2003). Contribution of the Patagonia Icefields of South America to sea level rise. *Science*, *302*(5644), 434-437.

Robertson Maurice, S. D., Wiens, D. A., Koper, K. D., & Vera, E. (2003). Crustal and upper mantle structure of southernmost South America inferred from regional waveform inversion. *Journal of Geophysical Research: Solid Earth*, *108*(B1).

Ruddiman, W. F., Raymo, M., & McIntyre, A. (1986). Matuyama 41,000-year cycles: North Atlantic Ocean and northern hemisphere ice sheets. *Earth and Planetary Science Letters*, *80*(1-2), 117-129.

Serpelloni, E., Faccenna, C., Spada, G., Dong, D., & Williams, S. D. (2013). Vertical GPS ground motion rates in the Euro-Mediterranean region: New evidence of velocity gradients at different spatial scales along the Nubia-Eurasia plate boundary. *Journal of Geophysical Research: Solid Earth*, *118*(11), 6003-6024.

Stern, C. R., & Kilian, R. (1996). Role of the subducted slab, mantle wedge and continental crust in the generation of adakites from the Andean Austral Volcanic Zone. Contributions to mineralogy and petrology, 123, 263-281.

Sternai, P. (2020). Surface processes forcing on extensional rock melting. *Scientific reports*, *10*(1), 1-13.

Sternai, P. (2023). Feedbacks between internal and external Earth dynamics. In *Dynamics of Plate Tectonics and Mantle Convection* (pp. 271-294). Elsevier.

Sternai, P., Sue, C., Husson, L., Serpelloni, E., Becker, T. W., Willett, S. D., Faccenna, C., Di Giulio, A., Spada, G., Jolivet, L., Valla, P., Petit, C., Nocquet, J.-M., Walpersdorf, A., & Castelltort, S. (2019). Present-day uplift of the European Alps: Evaluating mechanisms and models of their relative contributions. *Earth-Science Reviews*, *190*, 589-604.

Stuhne, G. R., & Peltier, W. R. (2015). Reconciling the ICE-6G_C reconstruction of glacial chronology with ice sheet dynamics: The cases of Greenland and Antarctica. *Journal of Geophysical Research: Earth Surface*, *120*(9), 1841-1865.

Sue, C., Delacou, B., Champagnac, J. D., Allanic, C., & Burkhard, M. (2007). Aseismic deformation in the Alps: GPS vs. seismic strain quantification. *Terra Nova*, *19*(3), 182-188.

Thorndycraft, V. R., Bendle, J. M., Benito, G., Davies, B. J., Sancho, C., Palmer, A. P., Fabel, D., Medialdea, A., & Martin, J. R. (2019). Glacial lake evolution and Atlantic-Pacific drainage reversals during deglaciation of the Patagonian Ice Sheet. *Quaternary Science Reviews*, *203*, 102-127.

Turcotte, D. L., & Schubert, G. (2002). *Geodynamics*. Cambridge university press.

van der Wal, W., Whitehouse, P. L., & Schrama, E. J. (2015). Effect of GIA models with 3D composite mantle viscosity on GRACE mass balance estimates for Antarctica. Earth and Planetary Science Letters, 414, 134-143.

Walpersdorf, A., Sue, C., Baize, S., Cotte, N., Bascou, P., Beauval, C., Collard, P, Daniel, G., Dyer, H., Grasso, J.-R., Hautecoeur, O., Helmstetter, A., Hok, S., Langlais, M., Menard, G., Mousavi, Z., Ponton, F., Rizza, M., Rolland, L., Souami, D., & Martinod, J. (2015). Coherence between geodetic and seismic deformation in a context of slow tectonic activity (SW Alps, France). *Journal of Geodynamics*, *85*, 58-65.

Watts, A. B. (2001). *Isostasy and Flexure of the Lithosphere*. Cambridge University Press.

Willis, M. J., Melkonian, A. K., Pritchard, M. E., & Rivera, A. (2012). Ice loss from the Southern Patagonian ice field, South America, between 2000 and 2012. *Geophysical research letters*, *39*(17).

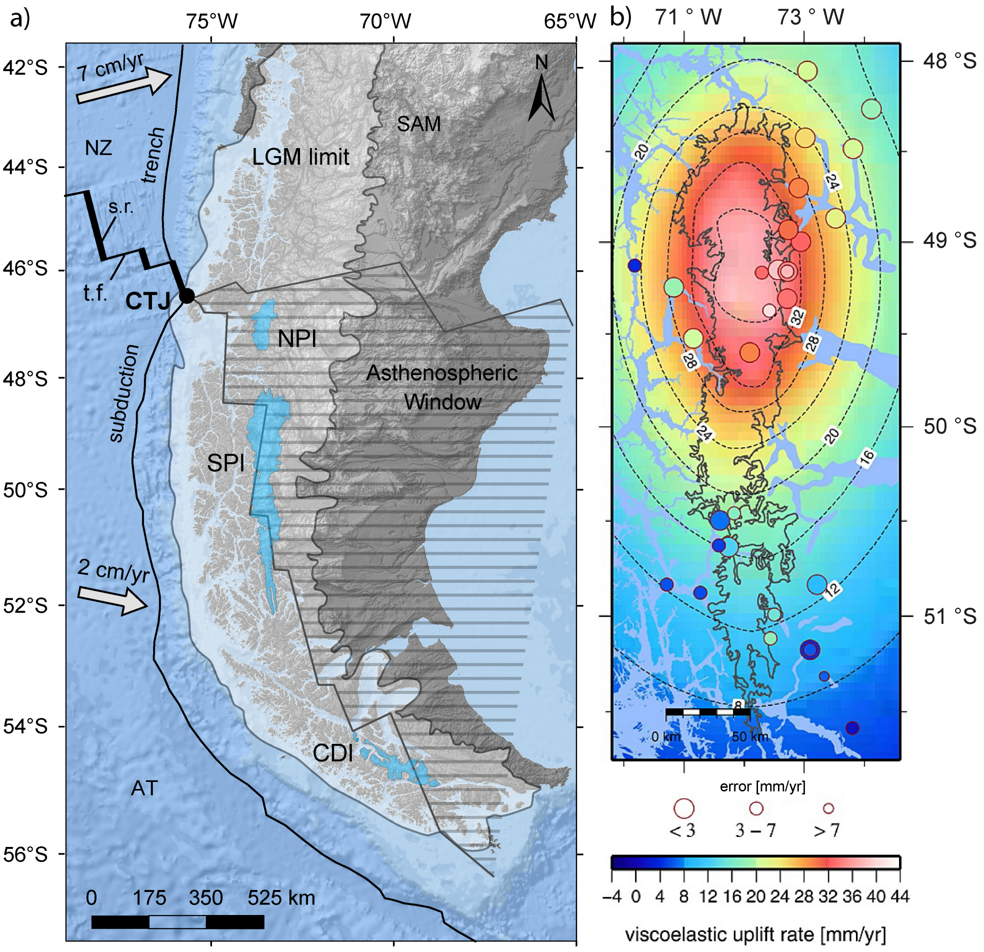

Fig. 1. Regional context and uplift rate data. a) Map of southern Patagonia with the Southern Patagonian Icefield (SPI), Northern Patagonian Icefield (NPI), and the Cordillera Darwin Icefield (CDI) in light blue, the approximate extension of the icefields at the Last Glacial Maximum (LGM limit), and the approximate extension of the present-day asthenospheric window (dashed region) beneath the South American Continent (SAM). In the Pacific Ocean, the spreading ridges (s.r., thick black lines) and transform faults (t.f., thin black lines) separate the Nazca (NZ) and the Antarctic (AT) plates. The subduction trench is also highlighted in black. The arrows show the approximate rate and direction of subduction of the oceanic plates. b) Zoom on the SPI with GPS stations (circles) used to estimate the viscoelastic uplift rates, from Lange et al. (2014).

https://doi.org/10.5194/egusphere-2023-1711
Preprint. Discussion started: 18 August 2023

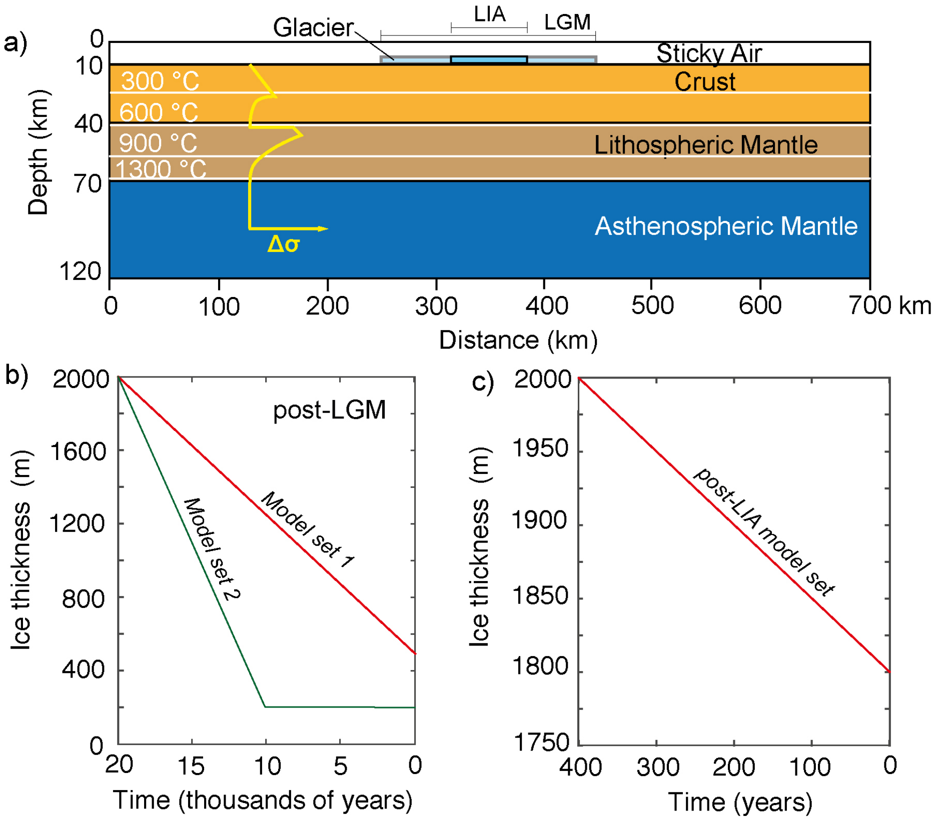

570 **Fig. 2. Reference numerical model setup.** a) Thermo-mechanical numerical model domain with rheological layers (Table 1), isotherms (white lines), and yield strength ($\Delta\sigma$) profile (yellow line). (b, c) Ice thickness vs. time used in the numerical models to simulate the post-LGM deglaciation in two model sets (b), and the post-LIA deglaciation (c).

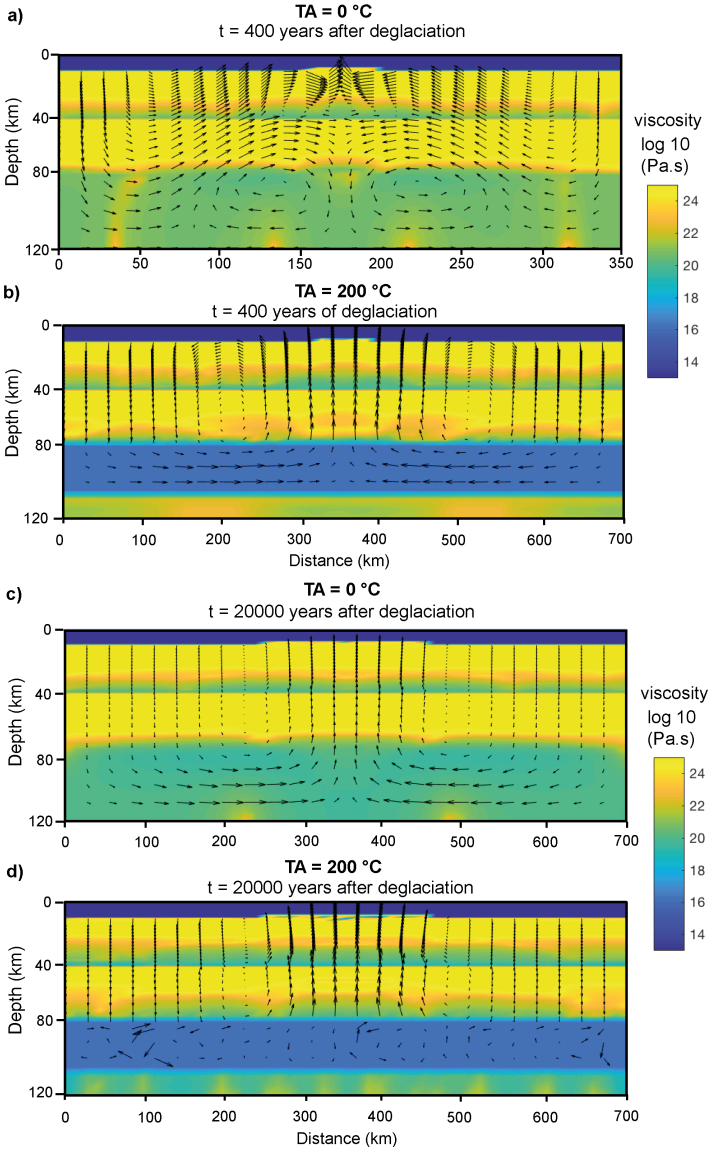

Fig. 3. Distribution of viscosity and velocity vectors in the numerical models. a) Reference model without an asthenospheric thermal anomaly, TA = 0 °C, and b) model with the higher simulated asthenospheric thermal anomaly, TA = 200 °C, in the last timestep of post-LIA deglaciation. c) Reference model with TA = 0 °C, and d) model with TA = 200 °C, in the last timestep of *Model set 1* of post-LGM deglaciation. Velocity vectors do not have the same scaling and are only meant for visualization purpose. 575

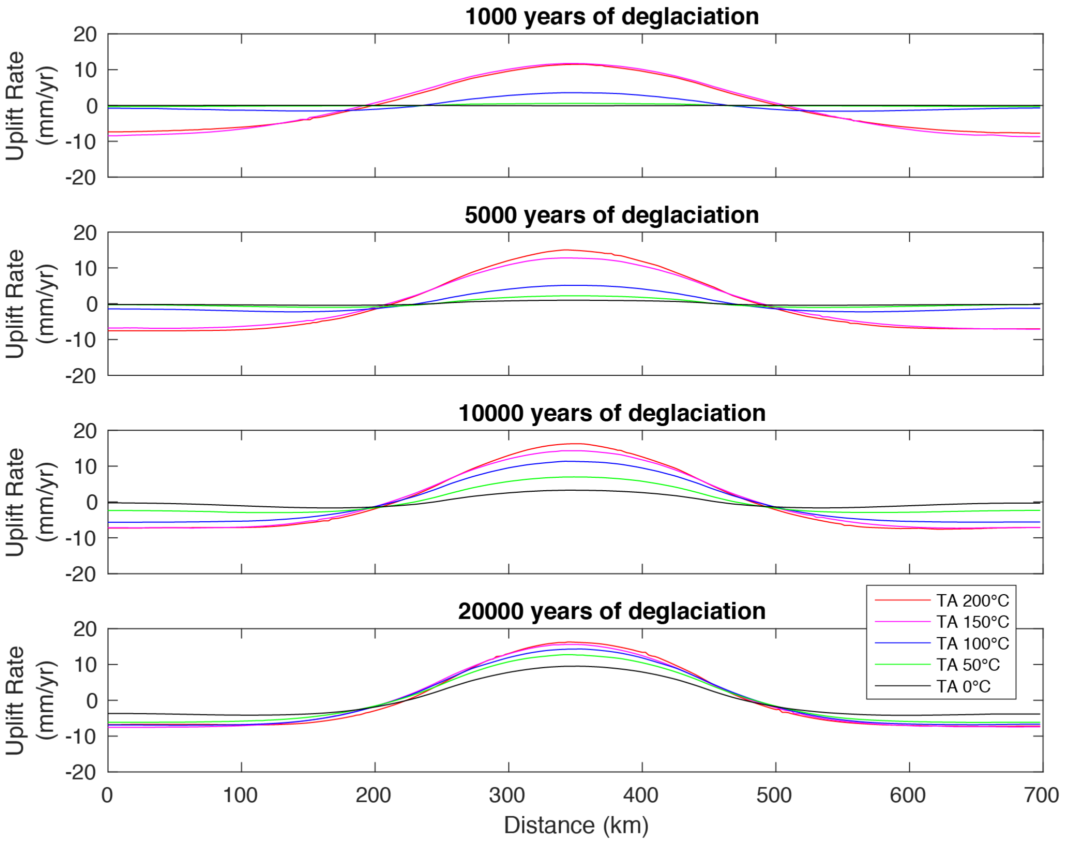

580 **Fig. 4. Surface uplift rates vs. distance for *Model set 1* of post-LGM deglaciation.** a) t = 1000 years of deglaciation, b) t = 5000 years of deglaciation, c) t = 10000 of deglaciation, d) 20000 years of deglaciation. Different line colours correspond to different TA.

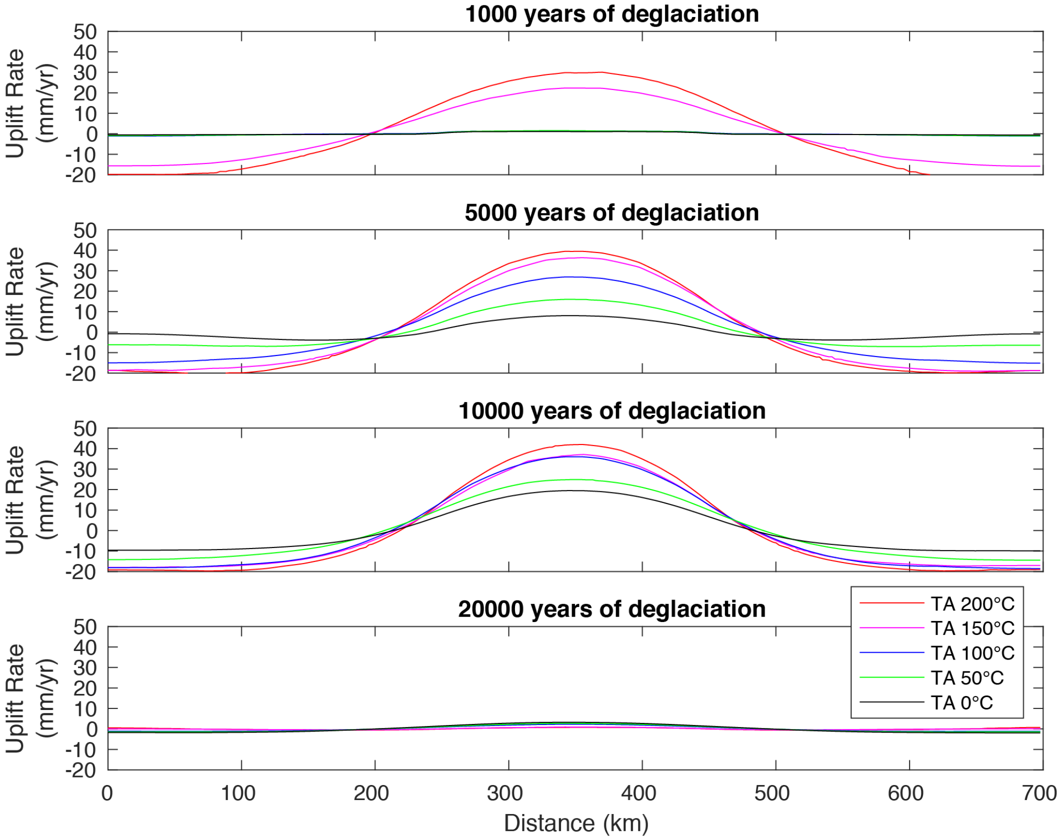

Fig. 5. Surface uplift rates vs. distance for *Model set 2* of post-LGM deglaciation. a) t = 1000 years of deglaciation, b) t = 5000 years of deglaciation, c) t = 10000 of deglaciation, d) 20000 years of deglaciation. Different line colours correspond to different TA.

585

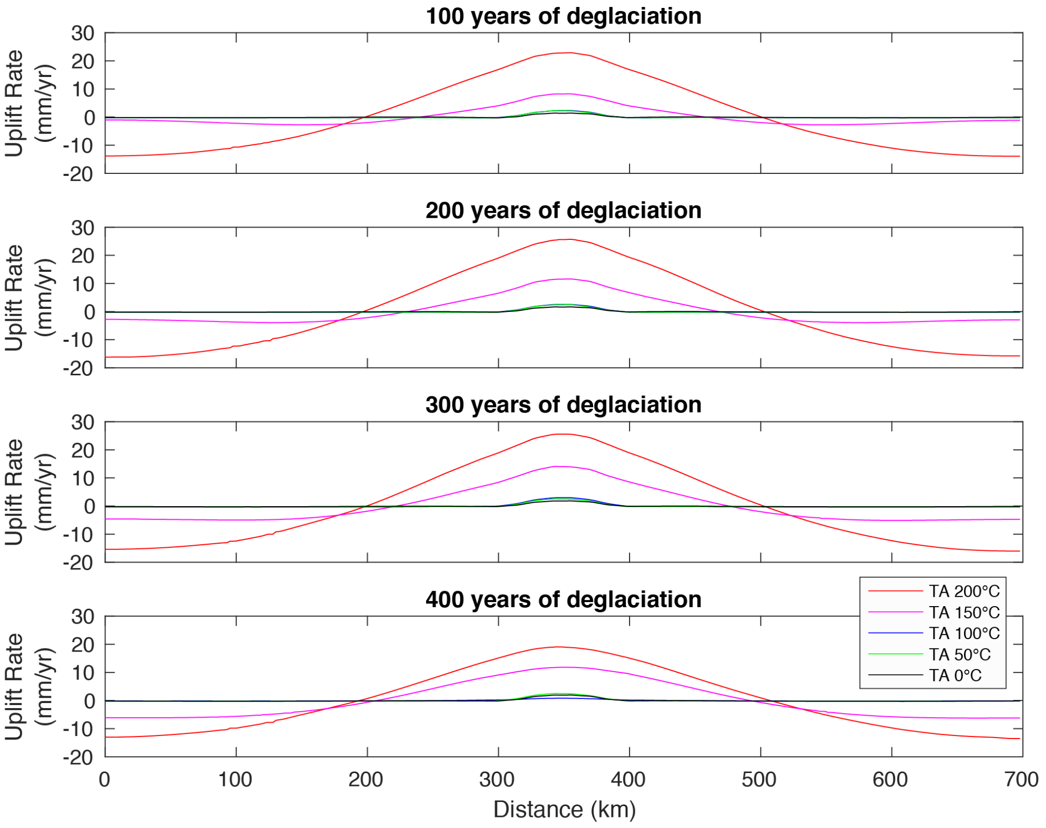

Fig. 6. Surface uplift rates vs. distance for post-LIA deglaciation model set. a) t = 100 years of deglaciation, b) t = 200 years of deglaciation, c) t = 300 years of deglaciation, d) 400 years of deglaciation. Different line colours correspond to different TA.

https://doi.org/10.5194/egusphere-2023-1711
Preprint. Discussion started: 18 August 2023

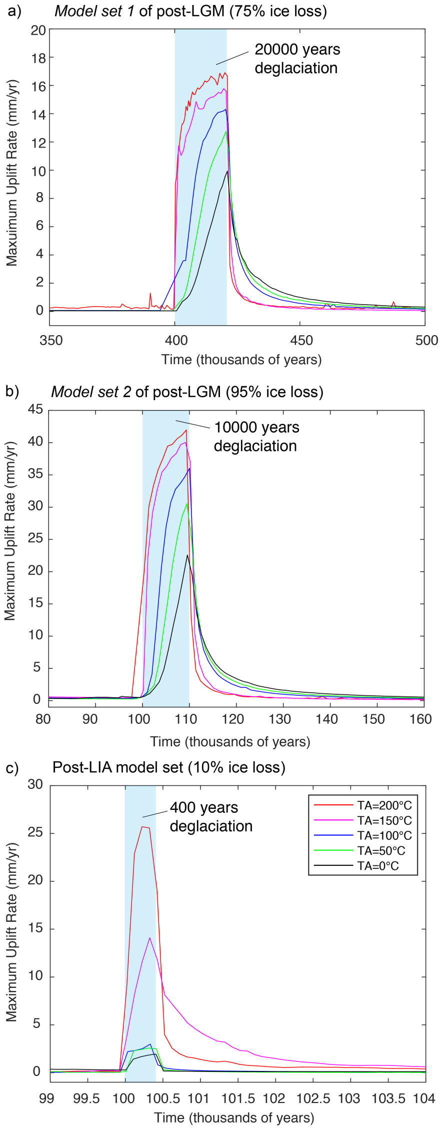

590 **Fig. 7. Maximum uplift rates vs. time for model sets of deglaciation with different TA.** a) *Model set 1* of post-LGM deglaciation accounting of 75% of ice loss in 20000 years, b) *Model set 2* of post-LGM deglaciation accounting of 95% of ice loss in 10000 years, and c) Post-LIA deglaciation model set accounting 10% of ice loss in 400 years (blue-shaded region). Blue-shaded regions highlight the modeled deglaciation intervals.

Table 1 – Material properties used in the numerical experiments.

	ρ_0^s (km/m^3)	E_a (kJ/mol)	V_a (m^3/mol)	n	C (Mpa)	*Visc.* flow law	*Sin* (ϕ_{eff})	*c* (W/m/K)	μ (Gpa)	C_p (J/kg/K)	*Hr* (µW/m^3)	H_l (kJ/kg)	α (1/k)	β (1/Pa)
Crust	2800	154	0	2.3	10	Wet Qz.	0.2	0.64+807/(T+77)	10	1000	1	300	$3x10^{-5}$	$1x10^{-11}$
Lithos-pheric mantle	3250	532	10	3.5	10	Dry Ol.	0.6	0.73+1293/(T+77)	67	1000	0.022	400	$3x10^{-5}$	$1x10^{-11}$
Asthenos-pheric mantle	3250	532	10	3.5	10	Dry Ol.	0.6	0.73+1293/(T+77)	67	1000	0.022	400	$3x10^{-5}$	$1x10^{-11}$
Ice	920	154	0	2.3	10		0	0.73+1293/(T+77)	67	1000	0.022	400	$3x10^{-5}$	$1x10^{-11}$

$\boldsymbol{\rho_0^s}$ is the standard densities of solid rocks; $\boldsymbol{E_a}$ is the activation energy; $\boldsymbol{V_a}$ is the activation volume; ***n*** is the stress exponent; ***C*** is cohesion; $\boldsymbol{\varphi_{eff}}$ is the effective internal friction angle; ***c*** is thermal conductivity; $\boldsymbol{\mu}$ is the shear modulus; $\boldsymbol{C_p}$ is the specific heat capacity; $\boldsymbol{H_r}$ and $\boldsymbol{H_l}$ are the radiogenic and latent heat productions, respectively; $\boldsymbol{\alpha}$ is thermal expansion; $\boldsymbol{\beta}$ is compressibility. Qz and Ol are quartzite and olivine, respectively. All rheological and partial melting laws/parameters are based on experimental rock mechanics and petrology (Ranalli, 1995; Hirschmann, 2000; Johannes, 1985; Turcotte and Schubert, 2002).

Table 2 – Maximum uplift rates derived from the numerical models with a thermal anomaly (TA) of 0, 50, 100, 150 and 200 °C for the *Model set 1* (a) and *Model set 2* (b) of post-LGM deglaciation, and the post-LIA deglaciation model set (c). The t = 0 is the timestep immediately before the beginning of deglaciation. Fig. 7 is a plot of the maximum uplift rate vs. time calculated for each timestep in all numerical models.

a) *Model set 1* of post-LGM deglaciation (20000 years)

TA (°C)	**Maximum uplift rate (mm/yr)**						
0	0.0425	0.0412	0.9781	3.2849	6.4337	9.5049	4.9781
50	0.0481	0.5650	2.2171	6.9983	10.7568	12.7473	4.6591
100	0.0674	3.5812	5.1450	11.3702	13.6265	14.3080	4.0696
150	0.0471	11.7188	12.7860	14.3219	15.1838	15.5924	1.3896
200	0.1513	11.4839	15.0235	16.2639	16.4590	16.2576	0.8946
	t = 0	**t = 1000 yr**	**t = 5000 yr**	**t = 10000 yr**	**t = 15000 yr**	**t = 20000 yr**	**t = 25000 yr**

b) *Model set 2* of post-LGM deglaciation (10000 years)

TA (°C)	**Maximum uplift rate (mm/yr)**						
0	0.5011	1.0885	8.0324	19.4849	5.6972	3.1222	2.1536
50	0.2527	1.5170	15.9284	24.8744	5.2380	2.7184	1.7310
100	0.3270	1.2905	26.9424	36.0223	4.9357	2.3015	1.4085
150	0.4273	22.3004	36.3278	37.1107	1.9319	0.9322	0.5953
200	0.3725	30.0494	39.4609	41.9771	1.4801	0.7525	0.4868
	t = 0	**t = 1000 yr**	**t = 5000 yr**	**t = 10000 yr**	**t = 15000 yr**	**t = 20000 yr**	**t = 25000 yr**

c) post-LIA deglaciation model set (400 years)

TA (°C)	**Maximum uplift rate (mm/yr)**						
0	0.4317	1.4151	1.6660	1.8366	1.9492	0.1764	0.1025
50	0.0352	2.2776	2.4264	2.5706	2.4514	0.3044	0.2340
100	0.0350	2.2024	2.3235	2.5241	2.9878	0.4854	0.3775
150	0.0933	8.2708	11.5730	14.0325	11.8261	8.1148	7.1503
200	0.0962	22.8938	25.7002	25.572	18.9666	3.9966	2.5535
	t = 0	**t = 100 yr**	**t = 200 yr**	**t = 300 yr**	**t = 400 yr**	**t = 500 yr**	**t = 600 yr**